

# A fine-grained parallelization of the immersed boundary method

Journal Title  
XX(X):1–14  
©The Author(s) 0000  
Reprints and permission:  
sagepub.co.uk/journalsPermissions.nav  
DOI: 10.1177/ToBeAssigned  
www.sagepub.com/

SAGE

Andrew Kassen<sup>1</sup>, Varun Shankar<sup>2</sup> and Aaron L. Fogelson<sup>1,3</sup>

## Abstract

We present new algorithms for the parallelization of Eulerian-Lagrangian interaction operations in the immersed boundary method. Our algorithms rely on two well-studied parallel primitives: key-value sort and segmented reduce. The use of these parallel primitives allows us to implement our algorithms on both graphics processing units (GPUs) and on other shared memory architectures. We present strong and weak scaling tests on problems involving scattered points and elastic structures. Our tests show that our algorithms exhibit near-ideal scaling on both multicore CPUs and GPUs.

## Keywords

CUDA, computational fluid dynamics, immersed boundary method, geometric modeling, red blood cell

## 1 Introduction

Many problems in biophysics involve the interaction of an incompressible fluid and an immersed elastic interface. The solution to these problems can be approximated using the immersed boundary (IB) method, which was developed in Peskin (1972) to simulate blood flow through the heart. The relative ease by which the IB method can be incorporated into a Navier-Stokes solver has led to its popularity in myriad applications (see, e.g. Mittal and Iaccarino (2005); Griffith and Patankar (2020) and references therein). The IB method couples the equations governing fluid velocity and pressure to those governing the interface movement and elastic forces via operations we will refer to as *interpolation* and *spreading*. Fluid velocities are interpolated to points on the interface, and forces on the interface are spread to the fluid. Fluid properties are discretized on a fixed Eulerian grid. The interface is represented by a set of mobile Lagrangian points. This presents a problem for effective parallelization of interpolation and spreading, as these operators must be reconstructed at each timestep to account for the motion of the Lagrangian points relative to the Eulerian grid. The Eulerian and Lagrangian points, on the other hand, can be treated as fixed in their respective coordinate spaces for several timesteps, if not for the entirety of a simulation. We may therefore treat solving the fluid equations and computing elastic forces as the result of a black-box computation and focus primarily on the interpolation and spreading operations.

We are interested in the case of neutrally buoyant, elastic immersed structures that move at the local fluid velocity. In particular, we aim to simulate whole blood, which is composed of red blood cells (RBCs) and platelets immersed in blood plasma, within a vessel lined by endothelial cells. The cells are elastic, and as they deform with the flow of the enveloping fluid, they impose a force on the fluid. Approximately 40% of the volume in healthy human blood

is occupied by RBCs, and domains containing just a few cells may require tens or hundreds of thousands of points to discretize these cells for use within the IB method.

To take advantage of modern computing architectures, with ever-increasing numbers of processors, it is necessary to develop parallel algorithms for the IB method. McQueen and Peskin (1997) present a domain decomposition scheme to parallelize the interpolation and spreading operations on the Cray C-90 computer with shared memory and a modest number of vector processors. Their results illustrate the need for a fast interpolation and spreading: even parallelized, they spend roughly half of the wall clock time spreading and interpolating. Fai et al. (2013) adapted this domain decomposition scheme for use on a general purpose graphical processing unit (GPGPU; GPU for short). Patel (2012) parallelized spreading on a GPU by processing one Lagrangian point at a time. Because neither of these approaches can concurrently process arbitrary Lagrangian points, it is easy to find cases for which they perform poorly. An alternative is to distribute work among several devices, each with its own memory. This idea underpins the popular IBAMR library (see Griffith et al. (2010, 2007); Griffith (2009, 2011); Griffith and Luo (2017)), which also adaptively refines the mesh around the immersed structure. With proper load-balancing, this allows a serial algorithm to process a smaller portion of work. A cluster of multicore devices, however, will not be used effectively without a shared-memory parallel algorithm. The cuIBM (Layton et al. (2011)) and PetIBM

<sup>1</sup>Department of Mathematics, University of Utah, Salt Lake City, UT, USA

<sup>2</sup>School of Computing, University of Utah, Salt Lake City, UT, USA

<sup>3</sup>Department of Biomedical Engineering, University of Utah, Salt Lake City, UT, USA

## Corresponding author:

Aaron L. Fogelson, 155 S 1400 E, JWB 233, Salt Lake City, UT 84112, USA

Email: fogelson@math.utah.edu

(Mesnard and Barba (2017); Chuang et al. (2018)) libraries implement an adaptive IB method for prescribed motion on single- and multi-GPU architectures, respectively. The authors demonstrate their method on a few two-dimensional test problems. Their implementation explicitly constructs the spreading and interpolation operators, which are sparse. The interpolation matrix has approximately the same number of nonzero entries per row, can be constructed in parallel in compressed sparse row (CSR) format, and its multiplication against a column vector parallelizes easily as a series of sparse dot products. The spreading matrix, with approximately the same number of nonzero entries per column, can be constructed in parallel in compressed sparse column (CSC) format, for which parallel multiplication against a column vector typically requires conversion to a different format. Even after conversion to CSR, the spreading matrix does not have approximately the same number of entries per row so does not always yield effective parallelization of matrix-vector products.

GPUs have restrictions on their parallelization. They use single instruction, multiple data (SIMD) parallelism, in which each computational unit, or thread, executes the same instruction on its own data. Concurrency on the GPU is typically limited by the amount of shared memory, which is shared among a group of threads, and register memory, which is accessible only to a single thread. The alternative is to use global memory, which is slow in general, but faster when accesses are sequential (or “coalesced”). These restrictions on the GPU imply that an effective algorithm for the GPU translates well to other shared-memory architectures, such such as multicore CPUs, which support parallelism, SIMD instructions, advanced instruction pipelining, and out-of-order execution. We therefore develop parallel spreading and interpolation algorithms applicable to both GPUs and multicore CPUs. The success of our new algorithms relies in dividing these operations into trivially parallelizable tasks and parallel primitives.

The remainder of this paper is organized into four sections. Section 2 gives an overview of the IB method, and describes the role of the interpolation and spread operations. In Section 3, we discuss the parallelization of interpolation and introduce a new parallelization for the spreading operation. In Section 4, we demonstrate that the concurrency of these algorithms scales with the number of IB points, independently of the Eulerian grid. We confirm the convergence of the IB method with these new algorithms. We illustrate the suitability of our algorithms to both GPUs and multicore CPU architectures with both weak and strong scaling tests. Finally, we summarize our findings in Section 5.

## 2 Review of the immersed boundary method

Consider a  $d$ -dimensional ( $d = 2$  or  $3$ ) rectangular domain  $\Omega$ , which is filled with a viscous incompressible fluid with constant viscosity  $\mu$  and density  $\rho$ , and contains an immersed elastic structure,  $\Gamma$ . The structure is impermeable to the fluid and moves at the local fluid velocity, is deformed by this motion, and imparts a force to the fluid. Otherwise, the interface is treated as part of the fluid.

The fluid velocity,  $\mathbf{u} = \mathbf{u}(\mathbf{x}, t)$ , and pressure,  $p = p(\mathbf{x}, t)$ , are governed by the incompressible Navier-Stokes equations for a Newtonian fluid,

$$\begin{aligned} \rho(\mathbf{u}_t + \mathbf{u} \cdot \nabla \mathbf{u}) &= \mu \Delta \mathbf{u} - \nabla p + \mathbf{f}, & (1) \\ \nabla \cdot \mathbf{u} &= 0, & (2) \end{aligned}$$

where  $\mathbf{f}$  is the elastic force density. This is a set of  $d + 1$  equations in  $d + 1$  unknowns: the  $d$  components of  $\mathbf{u}$ , and  $p$ . The equations are written relative to the Eulerian frame, so that the coordinates  $\mathbf{x}$  are independent variables. Throughout, we write Eulerian quantities in the lowercase Latin alphabet.

Let  $\mathbf{X} = \mathbf{X}(\boldsymbol{\theta}, t)$  represent a parametrization of the Cartesian coordinates of the immersed interface with material coordinates  $\boldsymbol{\theta}$  at time  $t$ . Let  $\mathcal{E}[\mathbf{X}]$  be the energy density functional for the elastic interface material. The elastic force density is computed by evaluating

$$\mathbf{F} = -\delta \mathcal{E}[\mathbf{X}], \quad (3)$$

where  $\delta$  represents the first variation. Uppercase Latin letters represent Lagrangian quantities and are functions of  $\boldsymbol{\theta}$  and  $t$ .

The interface moves at the local fluid velocity, and force balance on the interface between the interface and fluid dictates that the interface force on the fluid is equal to the elastic force. Analytically, the fluid-interface interactions can be written

$$\dot{\mathbf{X}}(\boldsymbol{\theta}, t) = \int_{\Omega} \delta(\mathbf{x} - \mathbf{X}(\boldsymbol{\theta}, t)) \mathbf{u}(\mathbf{x}, t) d\mathbf{x}, \quad (4)$$

$$\mathbf{f}(\mathbf{x}, t) = \int_{\Gamma} \delta(\mathbf{x} - \mathbf{X}(\boldsymbol{\theta}, t)) \mathbf{F}(\boldsymbol{\theta}, t) d\boldsymbol{\theta}, \quad (5)$$

where  $\dot{\mathbf{X}}(\boldsymbol{\theta}, t)$  represents the derivative of  $\mathbf{X}(\boldsymbol{\theta}, t)$  with respect to  $t$ , and  $\delta(\mathbf{x} - \mathbf{X}(\boldsymbol{\theta}, t))$  is the Dirac  $\delta$ -function centered at  $\mathbf{X}(\boldsymbol{\theta}, t)$ . Equation (4) is called *interpolation*, and the result of the right-hand side is the fluid velocity at  $\mathbf{X}(\boldsymbol{\theta}, t)$ ; namely,  $\dot{\mathbf{X}}(\boldsymbol{\theta}, t) = \mathbf{u}(\mathbf{X}(\boldsymbol{\theta}, t), t)$ . Equation (5) is called *spreading*.  $\mathbf{F}(\boldsymbol{\theta}, t)$  and  $\mathbf{f}(\mathbf{x}, t)$  may not have the same units, but the force  $\mathbf{F}(\boldsymbol{\theta}, t) d\boldsymbol{\theta}$  over  $d\boldsymbol{\theta}$  is “spread” to the force  $\mathbf{f}(\mathbf{x}, t) d\mathbf{x}$  over  $d\mathbf{x}$ .

The fluid equations (1)–(2) are spatially discretized on a regular background grid of spacing  $h$  so that  $\Omega$  is divided into square or cubic cells of side length  $h$ . Because of the checkerboard instability (see, e.g., Wesseling (2001)) in solving the Navier-Stokes equations on collocated regular grids, we use a MAC grid (Harlow and Welch (1965)) to stagger the components of Eulerian vector quantities. For example, if  $\mathbf{v}$  is an Eulerian vector-valued function,  $\mathbf{e} \cdot \mathbf{v}$  is discretized at  $\mathbf{x} - h\mathbf{e}/2$ . These discretization points comprise a new, regular grid with spacing  $h$ . For the component under consideration,  $\Omega_h$  denotes the set of discretization points with cardinality  $n_\omega$ . The momentum equation (1) is discretized in time using a first-order method based on the implicit-explicit Runge-Kutta method described in Peskin (2002), and the incompressibility condition (2) is satisfied using PmIII of Brown et al. (2001).

The Lagrangian force density (3) is evaluated at a set of points, usually with *fixed* material coordinates, referred to as IB points. The notation  $\mathbf{X}_j = \mathbf{X}(\boldsymbol{\theta}_j, t)$  refers to an

individual IB point on  $\Gamma$  in Cartesian coordinates. The typical heuristic for distributing the points  $\mathbf{X}_j$  on a connected interface places neighboring IB points at most  $h$  apart from one another, and often at most  $h/2$  apart. We therefore denote the set of IB points by  $\Gamma_h$  and the number of IB points by  $n_\gamma$ . From these points, we construct a smooth approximation to the interface using radial basis functions (RBFs), as in Shankar et al. (2015). This allows us to calculate geometric properties using well-known formulas, and evaluate the forces (3) in analytic form, similar to that of Maxian et al. (2018).

The singular integrals (4) and (5) do not lend themselves easily to evaluation. In particular, it is unlikely that IB points and grid points will coincide. For a regular grid with spacing  $h$ , we replace the Dirac  $\delta$ -function with a regularized kernel,  $\delta_h$ , which is a product of one-dimensional kernels,  $h^{-1}\phi(h^{-1}x)$ . Griffith and Patankar (2020) gives several options for  $\phi$ . The methods described in this paper do not depend on a particular  $\phi$ , but we restrict ourselves to the cosine kernel from Peskin (2002). The cosine kernel is simple to implement, but does not satisfy all of the moment conditions for a 4-point kernel, though it approximates a kernel with the appropriate discrete properties.

Let  $\Omega_h$  be one of the Eulerian grids for vector-valued quantities. Discretizing the component of equations (4) and (5) on  $\Omega_h$  and  $\Gamma_h$ , respectively, corresponding to canonical basis vector  $e$  yields

$$e \cdot \dot{\mathbf{X}}_j^n = \sum_{i=1}^{n_\omega} \delta_h(\mathbf{x}_i - \mathbf{X}_j^n) e \cdot \mathbf{u}_i^n h^d \quad \text{and} \quad (6)$$

$$e \cdot \mathbf{f}_i^n = \sum_{j=1}^{n_\gamma} \delta_h(\mathbf{x}_i - \mathbf{X}_j^n) e \cdot \mathbf{F}_j^n d\theta_j, \quad (7)$$

where  $\mathbf{u}_i^n$  and  $\mathbf{f}_i^n$  are discrete approximations to  $\mathbf{u}$  and  $\mathbf{f}$  at  $\mathbf{x}_i \in \Omega_h$  and time  $t = t_n$ , and  $\dot{\mathbf{X}}_j^n$  and  $\mathbf{F}_j^n$  are their Lagrangian counterparts at  $\mathbf{X}_j$ , respectively. The terms  $h^d$  and  $d\theta_j$  are integration weights analogous to  $d\mathbf{x}$  and  $d\theta$ . For a topologically spherical interface, we compute weights on the unit sphere using RBFs, using a simplified version of the method described in Fuselier et al. (2013), and use the Jacobian of the mapping between the sphere and interface to obtain  $d\theta_j$ . Both (6) and (7) look like a matrix-vector multiplication, so we define the *spreading matrix*  $\mathcal{S} = (\delta_h(\mathbf{x}_i - \mathbf{X}_j^n))$  with row  $i$  and column  $j$ . We call its transpose,  $\mathcal{S}^\dagger$ , the *interpolation matrix*. Collecting values  $e \cdot \mathbf{u}_i^n h^d$  at each grid point as  $\mathbf{v}^n$  and  $e \cdot \mathbf{F}_j^n d\theta_j$  at each IB point as  $\mathbf{G}^n$ , we rewrite equations (6) and (7) in matrix form as

$$\dot{\mathbf{X}}^n = \mathcal{S}^\dagger \mathbf{v}^n \quad \text{and} \quad (8)$$

$$\mathbf{f}^n = \mathcal{S} \mathbf{G}^n, \quad (9)$$

respectively.

Collectively, the equations (1)–(5) constitute the IB method, and while different implementations of the IB method use different spatial and temporal discretizations, surface representations, elastic models, or choice of  $\delta_h$ , a single step proceeds with timestep  $k$  roughly as follows:

- (a) interpolate  $\mathbf{u}^n$  to  $\mathbf{X}^n$  to get  $\dot{\mathbf{X}}^*$ ,
- (b) predict Lagrangian positions  $\mathbf{X}^* = \mathbf{X}^n + k\dot{\mathbf{X}}^*$ ,

- (c) compute Lagrangian forces  $\mathbf{F}^*$  using positions  $\mathbf{X}^*$ ,
- (d) spread  $\mathbf{F}^*$  from  $\mathbf{X}^*$  to get  $\mathbf{f}^*$ ,
- (e) solve for updated Eulerian velocities  $\mathbf{u}^{n+1}$ ,
- (f) interpolate  $\mathbf{u}^{n+1}$  to  $\mathbf{X}^n$  to get  $\dot{\mathbf{X}}^{n+1}$ , and
- (g) update  $\mathbf{X}^{n+1} = \mathbf{X}^n + k\dot{\mathbf{X}}^{n+1}$ .

We group these steps into 3 categories: the purely Eulerian (e); the purely Lagrangian (b), (c), and (g); and the Eulerian-Lagrangian coupling (a), (d), and (f). We discuss the first two categories in a forthcoming paper. The remainder of this paper discusses the implementation and parallelization of the third.

### 3 Parallelization strategies for interpolation and spreading

Here, we describe a method for evaluating the discrete counterparts to

$$E(\mathbf{X}) = \int_{\Omega} \delta_h(\mathbf{x} - \mathbf{X}) e(\mathbf{x}) d\omega \quad \text{and} \quad (10)$$

$$\ell(\mathbf{x}) = \int_{\Gamma} \delta_h(\mathbf{x} - \mathbf{X}) L(\mathbf{X}) d\gamma \quad (11)$$

where scalar-valued Eulerian function  $e : \Omega \rightarrow \mathbb{R}$  is interpolated to Lagrangian point  $\mathbf{X}$  and Lagrangian function  $L : \Gamma \rightarrow \mathbb{R}$  is spread to Eulerian point  $\mathbf{x}$ . For vector-valued functions, such as the Eulerian fluid velocity  $\mathbf{u}$  and Lagrangian force density  $\mathbf{F}$ , the algorithm can be applied to each component individually. For a staggered grid, this is necessary, as the grid for each component has a different set of grid points, and may have a different number of grid points. In the following, we discuss parallelizing equation (10) and introduce a novel parallelization scheme for evaluating equation (11). We begin by defining some notation that will be used throughout the description of these algorithms.

#### 3.1 Preliminaries

For a regular grid on  $\Omega$  with grid spacing  $h$ ,  $\Omega_h$ , any grid point  $\mathbf{x} \in \Omega_h$  can be decomposed into a vector  $\mathbf{i}$  with integer components and a fixed grid staggering,  $\mathbf{g} \in [0, 1)^d$ , such that  $\mathbf{x} = h(\mathbf{i} + \mathbf{g})$ . Let  $\Gamma_h$  be a discretization of the interface  $\Gamma$ . For the purposes of interpolation and spreading, we can think of  $\Gamma_h$  as a collection of arbitrary points in  $\Omega$ .

The kernel  $\delta_h$  is the tensor product of scaled, one-dimensional kernels,  $h^{-1}\phi(h^{-1}x)$ . Let  $\text{supp } \phi$  denote the support of  $\phi$  and define

$$s[\phi] = \max_{r \in [0, 1)} |\text{supp } \phi(\cdot - r) \cap \mathbb{Z}| - 1 \quad (12)$$

to be the size of the support in terms of unit intervals. For brevity, we write  $s = s[\phi]$ . For any  $\mathbf{X} \in \Omega$ , there are at most  $s^d$  grid points  $\mathbf{x} \in \Omega_h$  for which  $\delta_h(\mathbf{x} - \mathbf{X})$  is nonzero. We call these points the *support points* of  $\mathbf{X}$ . If  $\mathbf{X}$  is sufficiently far from any boundary, the set of points in  $\Omega$  with the same set of support points as  $\mathbf{X}$  is a region of  $\Omega$  the same size as a background grid cell. These regions partition  $\Omega$  and therefore contain at most one grid point. For  $\mathbf{X}$  near a non-periodic boundary, the region may be smaller, and may not contain a grid point. We extend the grid so that each of these

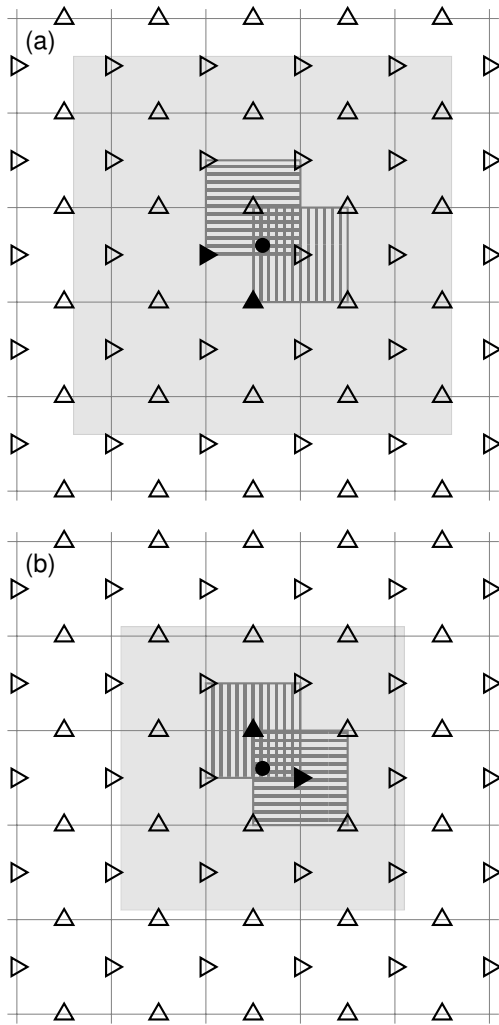


**Figure 1.** A region of a 2-dimensional domain containing point  $\mathbf{X}$ , indicated by a black circle. Light gray lines indicate physical units in increments of  $h$ , and  $\mathbf{X}$  has the same coordinates in each subfigure. Light gray boxes indicate the support of  $\delta_h(\cdot - \mathbf{X})$ . Subfigure (a) has  $s = 4$  support points in each dimension, and (b) has  $s = 3$ . The grid for horizontal vector components has staggering  $\mathbf{g} = (0, 0.5)$  and is marked by right-pointing triangles, whereas upright triangles mark the grid for vertical vector components and has staggering  $\mathbf{g} = (0.5, 0)$ . Those grid points within the gray boxes are also support points of  $\mathbf{X}$ . The horizontally- and vertically-stripped gray boxes denote the grid cell containing  $\mathbf{X}$  on the horizontal or vertical component grid, respectively. The filled triangles mark the point  $\mathbf{x} = h(\lfloor \mathbf{X} \rfloor + \mathbf{g})$ , corresponding to shift  $\boldsymbol{\sigma} = (0, 0)$  on the appropriate grid. The positions of the grid cells in (a) are typical of all even  $s$ , and the positions of the grid cells in (b) are typical of all odd  $s$ .

regions contains a single grid point. For the MAC grid, this means adding grid points to the boundary of  $\Omega$ , and is only strictly necessary for cases where grid points are not at a corner of a region, *i.e.*,  $s$  is odd. We call this extension  $\bar{\Omega}_h$ . We consider these regions to be the *de facto* grid cells, and henceforth refer to them as such. The striped gray boxes in Figure 1 therefore represent these cells, and illustrates the effect different choices of  $\phi$  has on their location. We can now identify any  $\mathbf{X} \in \Omega$  with a grid point  $\mathbf{x} \in \bar{\Omega}_h$  if they are in the same grid cell, and since  $\mathbf{x} = h(\mathbf{i} + \mathbf{g})$  is the only grid point in the grid cell, we identify the cell by the integers

---

**Algorithm 1** Shift construction
 

---

```

1: procedure SHIFT( $j, s, d$ )
2:   ▷ require:  $1 \leq j \leq s^d$ 
3:   ▷ generate: Shift  $\boldsymbol{\sigma}_j$ 
4:    $\boldsymbol{\sigma} \leftarrow \mathbf{0}$  ▷  $d$  zeros
5:   for  $i = 1, \dots, d$  do
6:      $\sigma_i \leftarrow \text{mod}(j - 1, s) - \lfloor s/2 \rfloor$ 
7:      $j \leftarrow \lfloor (j - 1)/s \rfloor$ 
8:   end for
9:   return  $\boldsymbol{\sigma}$ 
10: end procedure

```

---

*i.* We adopt the notation  $\lfloor \mathbf{X} \rfloor = \mathbf{i}$  for the function that maps points in  $\Omega$  to the vector of integers identifying the grid cell containing  $\mathbf{X}$ .

We now turn our attention to the evaluation of  $\delta_h(\mathbf{x} - \mathbf{X})$ . We assume  $\mathbf{x} \in \Omega_h$  and write

$$\begin{aligned} \delta_h(\mathbf{x} - \mathbf{X}) &\equiv \delta_h(h\boldsymbol{\sigma} - \Delta\mathbf{x}) \\ &= \prod_{i=1}^d h^{-1} \phi((\boldsymbol{\sigma} - h^{-1}\Delta\mathbf{x})_i), \end{aligned} \quad (13)$$

where  $\Delta\mathbf{x} = \mathbf{X} - h(\lfloor \mathbf{X} \rfloor + \mathbf{g})$  is the displacement of  $\mathbf{X}$  from its associated grid point,  $\boldsymbol{\sigma} = \lfloor \mathbf{x} \rfloor - \lfloor \mathbf{X} \rfloor$ , and subscript  $i$  denotes the  $i^{\text{th}}$  component. We refer to  $\boldsymbol{\sigma}$  as a *shift*. Shifts that result in a possibly nonzero value of  $\delta_h$  are known *a priori* based on the kernel  $\phi$ , and usually range from  $-\lfloor s/2 \rfloor$  to  $\lfloor (s-1)/2 \rfloor$  in each component. We can therefore assign an order to the shifts,  $\boldsymbol{\sigma}_1, \boldsymbol{\sigma}_2, \dots, \boldsymbol{\sigma}_{s^d}$ . For example, Algorithm 1 computes  $\boldsymbol{\sigma}_j$  given  $s$  and  $d$  in colexicographic order. We need only compute  $\Delta\mathbf{x}$  once to be able to compute all nonzero values of  $\delta_h(\mathbf{x} - \mathbf{X})$ .

We need one more ingredient to construct  $\mathcal{S}$ . We let  $\mathbf{x}_k$  be the  $k^{\text{th}}$  grid point, and for Eulerian function  $e(\mathbf{x})$ , we construct the vector  $\mathbf{e}$  with  $k^{\text{th}}$  entry  $e_k = e(\mathbf{x}_k)$ . Define the *grid indexing function*

$$\#(\mathbf{i}) = \begin{cases} k, & \lfloor \mathbf{x}_k \rfloor = \mathbf{i}, \mathbf{x}_k \in \Omega_h \\ \emptyset, & \text{otherwise.} \end{cases} \quad (14)$$

The value  $\emptyset$  indicates an Eulerian point outside of  $\Omega$ , does not have a corresponding row in  $\mathcal{S}$ , and therefore does not contribute to spreading or interpolation. We are now ready to construct  $\mathcal{S}$ . Let  $\mathbf{X}_j$  be an IB point. The  $j^{\text{th}}$  column of  $\mathcal{S}$  is zero except for up to  $s^d$  values where, for  $i = 1, \dots, s^d$ , if  $\#(\lfloor \mathbf{X}_j \rfloor + \boldsymbol{\sigma}_i) = k \neq \emptyset$ ,

$$\mathcal{S}_{kj} = \delta_h(h(\boldsymbol{\sigma}_i + \lfloor \mathbf{X}_j \rfloor + \mathbf{g}) - \mathbf{X}_j). \quad (15)$$

From a practicality standpoint, it is unnecessary to explicitly construct  $\mathcal{S}$ . We illustrate this with the serial spreading algorithm.

### 3.2 Serial spread

Algorithm 2 lists an example serial implementation of spreading in pseudocode. The overall structure consists of two loops: a loop over the (indices of) IB points, and a loop over the (indices of) shifts. From this, we see that for a fixed choice of  $\phi$ , and therefore  $s$ , the amount of work is  $\mathcal{O}(n_\gamma)$ , *i.e.*, independent of the Eulerian grid. The spread values

**Algorithm 2** Serial spread

---

```

1: procedure SEQ-SPREAD( $\Gamma_h, \Omega_h, \mathbf{L}$ )
2:    $\triangleright$  generate: Approximate values of  $\ell$  (Eq. (11)) at
      each point in  $\Omega_h$ 
3:   for  $i = 1, \dots, n_\gamma$  do  $\triangleright$  Loop over IB points
4:      $\mathbf{x} \leftarrow h(\lfloor \mathbf{X}_i \rfloor + \mathbf{g})$   $\triangleright \mathbf{X}_i \in \Gamma_h, \mathbf{x} \in \Omega_h$ 
5:      $\Delta \mathbf{x} \leftarrow \mathbf{x} - \mathbf{X}_i$ 
6:     for  $j = 1, \dots, s^d$  do  $\triangleright$  Loop over shifts
7:        $\boldsymbol{\sigma} \leftarrow \text{SHIFT}(j, s, d)$   $\triangleright$  Algorithm 1
8:        $w \leftarrow \delta_h(\Delta \mathbf{x} + h\boldsymbol{\sigma})$ 
9:        $k \leftarrow \#(\lfloor \mathbf{x} \rfloor + \boldsymbol{\sigma})$ 
10:      if  $k \neq \emptyset$  then
11:         $\ell_k \leftarrow \ell_k + w \cdot L_i$ 
12:      end if
13:    end for
14:  end for
15:  return  $\ell$ 
16: end procedure

```

---

are accumulated into a vector  $\ell$  (line 11). The target index,  $k$  (line 9), is computed using the grid indexing function, introduced in the previous section. Note that  $k$  depends on  $\boldsymbol{\sigma}_j$ , and  $\mathbf{x}$ , which in turn depends on  $\mathbf{X}_i$ , as seen on line 4. This means that  $k$  depends on both loop indices. There is no guarantee that unique pairs of the loop variables  $i$  and  $j$  will yield unique target indices. As a result, simply parallelizing one or both of the loops may lead to write contentions.

The property that runtime be independent of the Eulerian grid is desirable, as the number of IB points is often much fewer than the number of grid points. In other words, many grid cells will be empty of IB points, and unless they have nearby IB points, there is no useful work to be done for that grid cell. An algorithm that depends on the Eulerian grid will invariably involve wasted computational resources. We therefore aim to preserve the independence property. This is achieved straightforwardly for interpolation.

### 3.3 Parallelization of interpolation

By construction,  $\mathcal{S}$  has approximately equal number of nonzero entries per column. This means, that the interpolation matrix,  $\mathcal{S}^\dagger$ , has approximately equal number of nonzero entries per row. This property is beneficial for parallelization. Consider the  $i^{\text{th}}$  row of  $\mathcal{S}^\dagger$ , which corresponds to interpolating to IB point  $\mathbf{X}_i$  using the values at its support points. There are at most  $s^d$  values in that row, which correspond to the shifts that give a potentially nonzero value for  $\delta_h$ . Compute  $\mathbf{x} = h(\lfloor \mathbf{X}_i \rfloor + \mathbf{g})$ . Then  $\Delta \mathbf{x} = \mathbf{x} - \mathbf{X}_i$ . Since the shifts  $\{\boldsymbol{\sigma}_j\}$  are known beforehand, we can compute  $\delta_h(h\boldsymbol{\sigma}_j + \Delta \mathbf{x})$  and accumulate products

$$E_i = \sum_{\substack{j=1 \\ \#(\boldsymbol{\sigma}_j + \lfloor \mathbf{x} \rfloor) \neq \emptyset}}^{s^d} \delta_h(h\boldsymbol{\sigma}_j + \Delta \mathbf{x}) e_{\#(\boldsymbol{\sigma}_j + \lfloor \mathbf{x} \rfloor)},$$

where  $\#(i)$  is defined in Equation 14. This is done for each IB point, for a total work proportional to the number of IB points.

Assigning one thread per IB point (i.e., one thread per row), this calculation can be performed in parallel, and since the  $i^{\text{th}}$  thread writes to the  $i^{\text{th}}$  entry of  $\mathbf{E}$ , there are no write

**Algorithm 3** Parallel interpolation

---

```

1: procedure PAR-INTERPOLATE( $\Gamma_h, \Omega_h, \mathbf{e}$ )
2:    $\triangleright$  generate: Approximate values of  $\mathbf{E}$  (Eq. (10)) at
      each point in  $\Gamma_h$ 
3:   for  $i = 1, \dots, n_\gamma$  parallel do
4:      $\mathbf{x} \leftarrow h(\lfloor \mathbf{X}_i \rfloor + \mathbf{g})$   $\triangleright \mathbf{X}_i \in \Gamma_h, \mathbf{x} \in \Omega_h$ 
5:      $\Delta \mathbf{x} \leftarrow \mathbf{x} - \mathbf{X}_i$ 
6:      $v \leftarrow 0$   $\triangleright$  Accumulator
7:     for  $j = 1, \dots, s^d$  do
8:        $\boldsymbol{\sigma} \leftarrow \text{SHIFT}(j, s, d)$   $\triangleright$  Algorithm 1
9:        $w \leftarrow \delta_h(\Delta \mathbf{x} + h\boldsymbol{\sigma})$ 
10:       $k \leftarrow \#(\lfloor \mathbf{x} \rfloor + \boldsymbol{\sigma})$ 
11:      if  $k \neq \emptyset$  then
12:         $v \leftarrow v + w \cdot e_k$ 
13:      end if
14:    end for
15:     $E_i \leftarrow v$ 
16:  end for
17:  return  $\mathbf{E}$ 
18: end procedure

```

---

contentions. This can be seen on lines 12 and 15 in Algorithm 3, where the accumulation happens in a temporary variable which is ultimately written to  $\mathbf{E}$ . In this case, the target index depends only on the loop variable  $i$ , and we can safely parallelize over this loop. Because the number of products is approximately the same for each row, each thread does approximately the same amount of work. On architectures that enforce thread synchrony, such as GPUs, this means that we do not incur a penalty from having threads wait for other threads to finish.

Since each thread computes the appropriate  $\delta_h$ -weights for its own row, it is unnecessary to construct  $\mathcal{S}^\dagger$  explicitly. Except allocating memory for  $\mathbf{E}$ , all of the work for this algorithm is parallel, so we expect to see near-perfect scaling. Additionally, other than using the grid spacing  $h$  for scaling in various places, the evaluation of  $\delta_h$ , and information about boundaries, there is no dependence on the Eulerian grid. We now show how these properties can be maintained for the spreading operation.

### 3.4 Parallel spreading

We return now to spreading. Consider a fixed  $j$  in Algorithm 2 so  $\boldsymbol{\sigma}_j$  is fixed. If every IB point inhabits its own grid cell, the support point for each IB point corresponding to  $\boldsymbol{\sigma}_j$  is unique. In this case, we can spread to those support points without concern for write contentions. This is unlikely to occur in practice. On the other hand, if every IB point were in the same grid cell, values could be accumulated in parallel before being spread. This too is unlikely to occur in practice. We can instead employ the *segmented reduce* algorithm, which, given a list of values and a corresponding list of keys, will sum (reduce) consecutive values as long as their keys match. The result is a potentially shorter list of reduced values and a list of non-repeating keys, though they may not be unique within the list. Suppose we were able to order the keys and values so that repeated keys are listed consecutively. The result of reducing this sorted data is a list of unique keys and a list where all values with the same key are combined.

These observations lead us to assign a unique index to each grid cell, and, for each IB point, to use the index for the grid cell an IB point inhabits as its key. The list of keys is therefore identical for each shift. If all IB points in the same grid cell are listed consecutively, *i.e.*, all occurrences of key  $k$  in the list of keys are listed consecutively, then segmented reduce accumulates values spread from all IB points within the same grid cell for the given shift. This results in at most one value per grid cell, and we can write without contentions.

To ensure that repeated keys are listed consecutively, we use *key-value sort*, which, given a list of values and a corresponding list of keys, sorts values according to a partial ordering imposed on the keys. The result is a sorted list of keys and a permuted list of values, but key-value pairs remain unchanged. That the keys are ordered is not important, but all instances of a given key are grouped as a side-effect. Computing keys and values, sorting by key, and applying the segmented reduce algorithm once per shift spreads all values. But notice that sorting once per shift results in the same sorted list of keys each time. This also implies that values are permuted in the same manner for each shift. Instead of sorting values, we construct a permutation by sorting the indices of the IB points. We now need only sort once per spread operation, and using the permutation, we can construct the list of values in sorted order for each shift. Now, we apply segmented reduction to the sorted list of keys and newly constructed list of values. Because the order of the keys dictates the code path taken by segmented reduce, reduction proceeds identically for each shift, but with different data. We discuss this further in the next section. Finally, we write the reduced values to the output. Computing values, reducing, and writing for each shift completes the calculation.

Lastly, we need suitable way to generate keys. A function  $\kappa$  that generates keys should be 1-to-1 with grid cells, or alternatively, to points in  $\bar{\Omega}_h$ . For this reason, it is useful to formulate  $\kappa$  as a function of  $\mathbb{Z}^d$  and so  $\kappa(\lfloor \mathbf{X} \rfloor)$  gives the key for IB point  $\mathbf{X}$ . The requirement that  $\kappa$  be injective will, in general, invalidate the grid indexing function as an otherwise good choice, as it maps each ghost point in  $\bar{\Omega}_h$  to  $\emptyset$ . We can, however, use the key to compute grid indices: the point in  $\Omega_h$  with key  $k$  also has grid index  $\#(\kappa^{-1}(k))$ . Because  $\kappa$  is injective,  $\kappa^{-1}(k)$  is well-defined, and for shift  $\sigma$ ,  $\#(\kappa^{-1}(k) + \sigma)$  yields the appropriate target index for writing to the output vector. Putting these pieces together, we have a complete parallel spreading algorithm, listed in Algorithm 4 and illustrated in Figure 2.

Lines 3–7 of Algorithm 4 construct the permutation by constructing a list of keys and a list of the indices of IB points,  $1, 2, \dots, n_\gamma$ , and sorting the indices according to the keys. The  $i^{\text{th}}$  entry in the permuted list of indices gives the index of the  $i^{\text{th}}$  IB point in sorted order. On line 8, we define  $q$  to be the number of unique keys, which is also the number of reduced values to write. Since the list of sorted keys does not change for different shifts, we compute it once and reuse the value; see lines 20–26. Values, one per IB point, are computed and stored in a list  $\mathbf{V}$  on lines 12–18. These values are then input to the segmented reduce, line 19.

Algorithm 4 does not explicitly depend on the Eulerian grid, with some caveats dependent upon implementation details. Our implementation relies on the `thrust` library

---

**Algorithm 4** Parallel spread
 

---

```

1: procedure PAR-SPREAD( $\Gamma_h, \Omega_h, \mathbf{L}$ )
2:    $\triangleright$  generate: Approximate values of  $\ell$  (Eq. (11)) at
      each point in  $\Omega_h$ 
3:   for  $i = 1, \dots, n_\gamma$  parallel do  $\triangleright$  Loop over IB points
4:      $K_i \leftarrow \kappa(\lfloor \mathbf{X}_i \rfloor)$   $\triangleright$  Sort key
5:      $P_i \leftarrow i$   $\triangleright$  Initial ordering
6:   end for
7:   sort  $\{P_i\}$  by  $\{K_i\}$   $\triangleright i \rightarrow P_i$  is a permutation
8:    $q \leftarrow$  count unique  $\{K_i\}$ 
9:   for  $j = 1, \dots, s^d$  do  $\triangleright$  Loop over shifts
10:     $\{K'_i\} \leftarrow \{K_i\}$ 
11:     $\sigma \leftarrow$  SHIFT( $j, s, d$ )  $\triangleright$  Algorithm 1
12:    for  $i = 1, \dots, n_\gamma$  parallel do  $\triangleright$  Loop over IB points
13:       $p \leftarrow P_i$ 
14:       $\mathbf{x} \leftarrow h(\lfloor \mathbf{X}_p \rfloor + \mathbf{g})$   $\triangleright \mathbf{X}_p \in \Gamma_h, \mathbf{x} \in \Omega_h$ 
15:       $\Delta \mathbf{x} \leftarrow \mathbf{x} - \mathbf{X}_i$ 
16:       $w \leftarrow \delta_h(\Delta \mathbf{x} + h\sigma)$ 
17:       $V_i \leftarrow w \cdot L_p$ 
18:    end for
19:    reduce  $\{V_i\}$  by  $\{K'_i\}$   $\triangleright$  Segmented reduce
20:    for  $i = 1, \dots, q$  parallel do  $\triangleright$  Loop over inhabited grid cells,  $q \leq n_\gamma$ 
21:       $\mathbf{x} \leftarrow h(\kappa^{-1}(K'_i) + \mathbf{g})$ 
22:       $m \leftarrow \#(\lfloor \mathbf{x} \rfloor + \sigma)$   $\triangleright \lfloor \mathbf{x} \rfloor \equiv \kappa^{-1}(K'_i)$ 
23:      if  $m \neq \emptyset$  then
24:         $\ell_m \leftarrow \ell_m + V_i$ 
25:      end if
26:    end for
27:  end for
28:  return  $\ell$ 
29: end procedure

```

---

to provide the key-value sort, segmented reduce, and unique counting routines. Sorting is implemented as radix sort, which has a runtime of  $\mathcal{O}(wn_\gamma/p)$ , where  $p$  is the number of processors/threads, and  $w$  is the number of bits required to represent every key. In general,  $w \propto \log_2 n$ , for  $n$  elements to be sorted, but we use 32-bit integers for keys, so  $w = 32$ . It is reasonable to assume that this is true for most use-cases, as there are approximately  $n_\omega$  possible keys, and implementations of BLAS and LAPACK typically use 32-bit integers for indexing. However, extremely fine grids with more than  $2^{32}$  grid points will require a larger data type to represent each key uniquely. In that case,  $w$  increases with a finer grid. Segmented reduction has a much more complicated relationship with the Eulerian grid. Parallelized segmented reduction has a worst-case runtime of  $\mathcal{O}(n_\gamma/p)$ , but the constant of proportionality depends on the density of IB points within inhabited grid cells. On the one hand, if all IB points inhabit the same grid cell, segmented reduce proceeds as a regular reduce, which is very fast. On the other hand, if every IB point inhabits its own grid cell, there is no work to be done, and any time spent by the algorithm is for naught. The density of IB points also affects the value of  $q$ , but is bounded above by  $n_\gamma$ . For up to  $2^{32}$  grid points, we expect the overall runtime of the spreading algorithm to be  $\mathcal{O}(n_\gamma/p)$ .

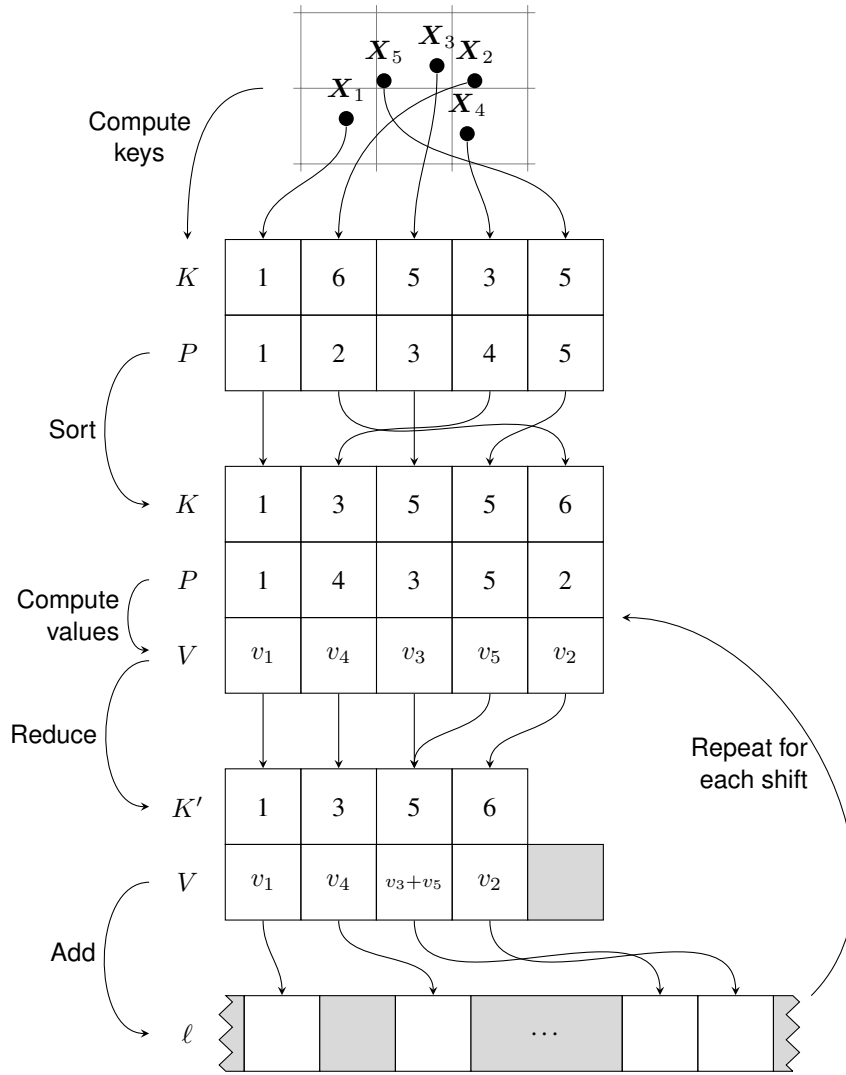


**Figure 2.** Schematic of Algorithm 4 for Lagrangian points  $X_1$  through  $X_5$  in a small region of  $\Omega$ . Gray grid lines indicate the boundaries of grid cells. The rows labelled  $K$ ,  $P$ ,  $V$ , and  $\ell$  represent the memory of arrays for the keys, permutation, values, and output vector, respectively. Keys are computed according to grid cell, starting with 1 at the bottom left and continuing sequentially from left to right then bottom to top. The value  $v_i$  corresponds to point  $X_i$  for a given shift, and are computed in sorted order using the values in  $P$ . The results of reducing  $V$  by  $K$  yields unique keys  $K'$ . Points  $X_3$  and  $X_5$  inhabit the same grid cell, so reduction adds their corresponding values before writing to the output vector. Gray regions denote unused memory.

Finally, we remark that Algorithm 4 must synchronize threads once per shift. For choices of  $\phi$  where  $s^d$  is large, this can hurt performance. This requirement is written as a parallel loop (line 12) within a serial loop (line 9). To reduce the number of synchronizations, we must be able to compute and store several values at once. However, attempting to write multiple values of once may lead to contentions. Below, we develop algorithms that require fewer synchronizations by using more memory to spread several values at once and avoid write contentions.

### 3.5 Buffered spreading variants

Here we introduce a buffer in which to store incomplete calculations. It can be thought of as a set of temporary output vectors, which we will combine at the end of the algorithm to finish the calculation. These vectors have  $n_\omega$  entries, so adding them requires as many operations, but is quite easily parallelized, and is provided by any parallel

BLAS implementation. In this regard, these buffered variants depend explicitly on the Eulerian grid. The only additional requirement is that there is enough memory to hold the buffer.

To develop these variants, we note that the sorted list of keys and the permutation are the same for all shifts. Since the permutation dictates the order of the values to spread, and the list of keys decides the behavior of the segmented reduce, these steps are nearly identical for each shift, save for the effect each shift might have on the values. We can therefore use several shifts to compute one value of  $\delta_h$  each, and use the same machinery to accumulate the values as if they were vectors. Then, to avoid write contentions, each of the entries of the reduced vectors is written to a separate output vector of the buffer. We choose  $s_z \approx 10$  values to compute each iteration. Summing the vectors in the buffer yields the desired result.

Algorithm 5 lists the general form of the algorithm as pseudocode, and Algorithm 6 gives a minor modification.

**Algorithm 5** Pre-allocated buffer parallel spreading

---

```

1: procedure PA-PAR-SPREAD( $\Gamma_h, \Omega_h, \mathbf{L}, \ell_1, \dots, \ell_{sz}$ )
2:    $\triangleright$  require:  $sz \geq 1$ 
3:    $\triangleright$  generate: Approximate values of  $\ell$  (Eq. (11)) at
      each point in  $\Omega_h$ 
4:   for  $i = 1, \dots, n_\gamma$  parallel do
       $\triangleright$  Loop over IB points
5:      $K_i \leftarrow \kappa(\lfloor \mathbf{X}_i \rfloor)$ 
       $\triangleright$  Sort key
6:      $P_i \leftarrow i$ 
       $\triangleright$  Initial ordering
7:   end for
8:   sort  $\{P_i\}$  by  $\{K_i\}$ 
       $\triangleright i \rightarrow P_i$  is a permutation
9:    $q \leftarrow \text{count unique } \{K_i\}$ 
10:  for  $j = 0, \dots, \lceil s^d/sz \rceil - 1$  do
       $\triangleright$  Loop over shifts
11:     $\{K'_i\} \leftarrow \{K_i\}$ 
12:    for  $i = 1, \dots, n_\gamma$  parallel do
       $\triangleright$  Loop over IB points
13:       $p \leftarrow P_i$ 
14:       $\mathbf{x} \leftarrow h(\lfloor \mathbf{X} \rfloor + \mathbf{g})$ 
       $\triangleright \mathbf{X}_p \in \Gamma_h, \mathbf{x} \in \Omega_h$ 
15:       $\Delta \mathbf{x} \leftarrow \mathbf{x} - \mathbf{X}_i$ 
16:      for  $k = 1, \dots, \min(sz, s^d - sz \cdot j)$  do
17:         $\sigma \leftarrow \text{SHIFT}(sz \cdot j + k, s, d)$ 
       $\triangleright$  Algorithm 1
18:         $w \leftarrow \delta_h(\Delta \mathbf{x} + h\sigma)$ 
19:         $V_{ik} \leftarrow w \cdot L(\mathbf{X}_p)$ 
       $\triangleright V \in \mathbb{R}^{n_\gamma \times sz}$ 
20:      end for
21:    end for
22:    reduce  $\{V_i\}$  by  $\{K'_i\}$ 
23:    for  $i = 1, \dots, q$  parallel do
       $\triangleright$  Loop over inhabited grid cells,  $q \leq n_\gamma$ 
24:       $\mathbf{x} \leftarrow h(\kappa^{-1}(K'_i) + \mathbf{g})$ 
25:      for  $k = 1, \dots, \min(sz, s^d - sz \cdot j)$  do
26:         $\sigma \leftarrow \text{SHIFT}(sz \cdot j + k, s, d)$ 
       $\triangleright$  Algorithm 1
27:         $m \leftarrow \#(\lfloor \mathbf{x} \rfloor + \sigma)$ 
28:        if  $m \neq \emptyset$  then
29:           $\ell_{mk} \leftarrow \ell_{mk} + V_{ik}$ 
30:        end if
31:      end for
32:    end for
33:  end for
34:  return  $\sum_{k=1}^{sz} \ell_k$ 
35: end procedure

```

---

**Algorithm 6** On-the-fly buffer parallel spreading

---

```

1: procedure OTF-PAR-SPREAD( $\Gamma_h, \Omega_h, \mathbf{L}$ )
2:    $\triangleright$  require:  $sz \geq 1$ 
3:    $\triangleright$  generate: Approximate values of  $\ell$  (Eq. (11)) at
      each point in  $\Omega_h$ 
4:   for  $i = 1, \dots, sz$  do
5:      $\ell_k \leftarrow \mathbf{0}$ 
6:   end for
7:   return PA-PAR-SPREAD( $\Gamma_h, \Omega_h, \mathbf{L}, \ell_1, \dots, \ell_{sz}$ )
       $\triangleright$  Algorithm 5
8: end procedure
       $\triangleright$  Lifetime of  $\ell_k$  ends here

```

---

The difference between these two variants is the lifetime of the buffer: Algorithm 5 does not manage the buffer itself, but Algorithm 6 allocates and frees the buffer memory, limiting the lifetime of the buffer to the duration of the algorithm.

The latter considers the memory allocation as part of the algorithm. The additional overhead from buffer allocation means that we never expect Algorithm 6 to outperform Algorithm 5; it is provided as an alternative for systems where maintaining a large, long-lived buffer may exhaust memory. We compare these algorithms and Algorithm 4 to Algorithm 2, and the efficacy of Algorithm 3 below.

## 4 Numerical results

Here we describe two types of test: unstructured IB points, in which points are placed randomly in the domain and generate a force independently from the other IB points, and structured IB points, in which the points comprise an elastic structure and forces are generated based on the configuration of the points as a whole. For these tests, we use a  $16 \mu\text{m} \times 16 \mu\text{m} \times 16 \mu\text{m}$  triply periodic domain with an initially shear-like flow,  $\mathbf{u} = (0, 0, \dot{\gamma}(y - 8 \mu\text{m}))$ , with shear rate  $\dot{\gamma}$ . Tests use a shear rate of  $1000\text{s}^{-1}$  unless otherwise noted. This flow has a sharp transition at the periodic boundary  $y = 0 \mu\text{m}$ , so a background force is added to maintain this transition and so that the initial flow is also the steady flow in the absence of other forces.

Serial and multicore CPU tests were performed on a single node with 48 Intel® Xeon® CPU E5-2697 v2 2.70GHz processors and 256 GB of RAM running CentOS Linux release 7.7.1908 (x86\_64). Parallel CPU implementations use Intel's OpenMP library, `libiomp5`. GPU tests used the same node with an NVIDIA® Tesla® K80 (2×GK210 GPU with 13 823.5MHz multiprocessors and 12 GB of global memory each). Only one of the GK210 GPUs was used. The CPU code was written in C++20 and the GPU code was written in C++/CUDA and used version 9.2 CUDA libraries (Kassen (2021)). Both the CPU and GPU code were compiled using `clang` version 7.0.1. All tests are performed in double precision. We begin with tests using unstructured IB points, for which both of these architectures were used.

### 4.1 Unstructured IB points

Consider a set of  $n$  IB points randomly placed in the domain described above. The IB points are imagined to be tethered to their initial positions. The fluid solver is not invoked for these tests. Instead, at each timestep, we interpolate the fluid velocity to each of the IB points and predict updated positions for the IB points. Using these predicted positions, we compute a Hookean force for each IB point with spring constant  $0.01\text{dyn/cm}$ . We spread these forces from the predicted positions to the fluid grid, but do not use them to update the fluid velocity. This ensures that the points do not settle into a steady position so the spreading and interpolation operations receive new data each timestep. Finally, we interpolate the velocity to the positions of the IB points at the beginning of the timestep again and update the position of the IB points. While the interpolated velocities are the same as those computed at the beginning of the timestep, this is done by analogy to the fluid solver, which interpolates fluid velocities twice and spreads forces once per timestep.

We use this test to compare the performance of the parallel algorithms to their serial counterparts and, for the spreading variants, to each other.

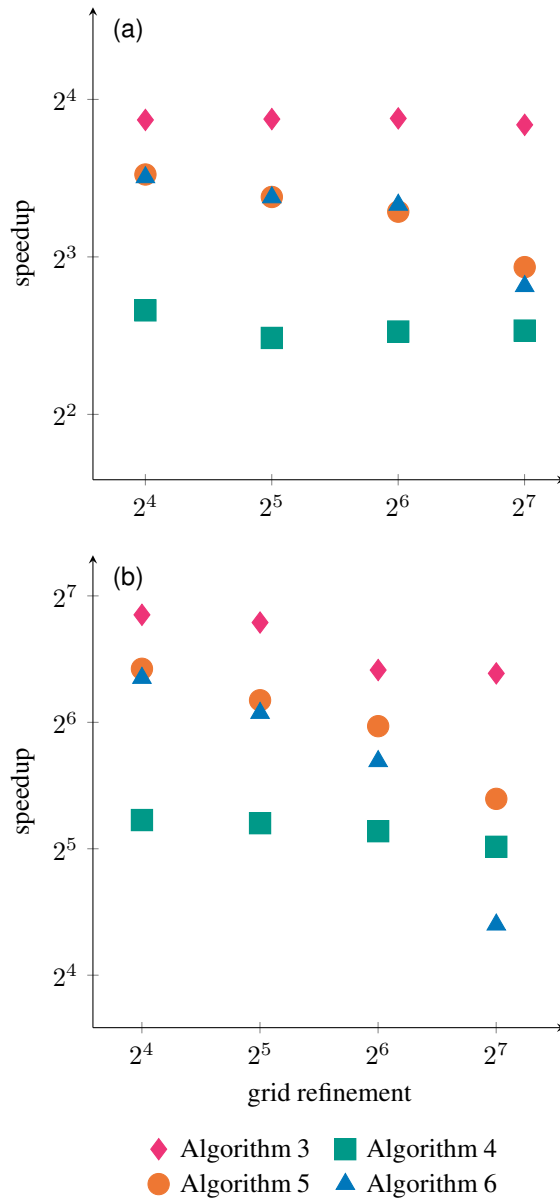
**4.1.1 Dependence on background grid** The serial Algorithms 2 and 3 do not explicitly depend on the size of the fluid grid. With perhaps the exception of the sorting and reducing steps, Algorithm 4 also does not depend on the size of the grid. Algorithms 5 and 6, on the other hand, ultimately sum their buffer vectors, which have one entry per grid point. Algorithm 6 also incorporates the allocation of these buffers. Using a few different fluid grids, we investigate whether Algorithms 3 and 4 are independent of the grid in practice, and how the grid dependence affects the runtime of Algorithms 5 and 6.

Table 1 lists timing results for  $n = 2^{16}$  IB points and 16, 32, 64, and 128 grid points per  $16 \mu\text{m}$ . The rows with device listed as  $1 \times \text{CPU}$  correspond to the serial algorithms and will serve as a reference point for the rest of the section. If the serial algorithms depend on the fluid grid, they do so only mildly. In fact, under close scrutiny, it seems that these deviations are due to hardware-level differences in the integer multiplications and additions used in computing sort keys and grid indices. We can therefore expect each of the algorithms to exhibit a mild variation in runtime for different grid refinements.

The speedup for these schemes is illustrated in Figure 3. Algorithm 3 is independent of the fluid grid, as expected. Any grid dependence introduced by the sort and reduce steps of Algorithm 4 is not obvious for the grids presented. On the other hand, the degradation of speedup for the sweep-fused Algorithms 5 and 6 is apparent for finer grids. For small problems with  $128^3$  or fewer grid points, one gets better performance from the sweep-fused variants, with the exception of Algorithm 6 on the GPU. This can be attributed to the slower allocation of the buffer for a finer grid. For problems where the grid has  $256^3$  or more grid points, we expect Algorithm 4 to be the fastest choice for spreading. Because our fluid solver fits in GPU memory only for fewer than  $128^3$  grid points, for the remainder of this work we consider only a grid with a grid refinement of 64 ( $h = 0.25 \mu\text{m}$ ). We can imagine using this algorithm on a less capable device with more limited memory, so we restrict ourselves to Algorithm 6 for spreading, computing  $s_z = 8$  values per sweep, to minimize the lifetime of the buffer used in spreading while still enjoying the benefit of using the buffer.

**4.1.2 Strong scaling** It is commonly the case that one wishes to employ parallelization to improve runtimes for a problem of interest. To illustrate this improvement, we now consider how runtime varies for the test problem with  $n = 2^{16}$  IB points, a grid refinement of 64 (grid size  $h = 0.25 \mu\text{m}$ ), and Algorithm 6 with different numbers of threads. We use up to 32 threads on the CPU and 64–4096 threads on the GPU. For a fixed problem, we ideally wish to see the runtime using  $2p$  threads to be half of that using  $p$  threads. In other words, using twice as many threads yield an ideal speedup of 2.

Figure 4 shows the results of these tests. Speedup is measured relative to the serial interpolation and spreading implementations. The trendlines estimate that increasing computing resources by a factor of two decreases runtime by a factor of about 1.91 for CPU and GPU interpolation and by a factor of about 1.85 for CPU spreading. It is not trivial to



**Figure 3.** Speedup of Algorithm 3 (interpolation) and Algorithms 4–6 (spreading) compared to their serial counterparts on  $2^{16}$  randomly placed IB points for different grid refinements on (a) 16 CPUs and (b) the GPU.

limit the number of threads used by `thrust` for work done on the GPU, so the key-value sort and segmented reduce use as many threads as `thrust` decides is prudent. While the trendline indicates a decrease in runtime by a factor of 1.91 as well, this is merely an approximation.

Parallel CPU interpolation using a single processor is identical to the serial CPU interpolate, so the CPU interpolate passes through  $(1, 1)$ . The same is not true of parallel spreading using a single processor compared to serial spreading. Because of the additional sort step in the parallel spreading algorithm, single-threaded Algorithm 4 is about 12% slower than its serial counterpart. The CPU code also enjoys the benefit of using vector registers for some of the computation. The GPU requires 64 threads to match the speed of a single CPU core. Even at 4096 threads, interpolate on the GPU shows no indication of plateauing. The final data point for that curve shows a speedup of approximately  $77 \times$ .

**Table 1.** Average timing results for interpolating to and spreading from  $2^{16}$  IB points from 1000 timesteps on different devices and grid configurations. Interpolation (Algorithm 3) happens twice per timestep and spreading (Algorithms 2, 4–6) happens once per timestep. Grid refinement is the number of grid points per  $16\ \mu\text{m}$  in each dimension. Times per call to the listed algorithm are reported in seconds.

Device	Algorithm	Grid refinement			
		16	32	64	128
$1 \times \text{CPU}$	2	1.33249	1.33621	1.33840	1.37281
	3	1.29633	1.31373	1.30763	1.35101
$16 \times \text{CPU}$	3	0.09890	0.09928	0.09974	0.10624
	4	0.23282	0.26431	0.25783	0.26590
	5	0.12803	0.14213	0.15215	0.20107
	6	0.12965	0.14242	0.14766	0.21874
$1 \times \text{GPU}$	3	0.01253	0.01317	0.01722	0.01816
	4	0.03930	0.04020	0.04215	0.04755
	5	0.01715	0.02049	0.02370	0.03656
	6	0.01804	0.02198	0.02873	0.07288

Figure 3(b), on the other hand, shows that the maximum speedup we can expect for this problem is approximately  $85\times$ , which the trendline in Figure 4(b) predicts will occur at approximately 4480 threads. Thus, we can expect the plateau for interpolate on the GPU to be very abrupt. This indicates a hardware limitation, the likely culprit being exhaustion of register memory. The plateauing of the CPU curves is not a limitation of the algorithm for the CPU. Despite having 48 cores, the test using 32 cores did not utilize them at full capacity. Using fewer cores, on the other hand, was able to maintain full utilization for the duration of the test. If not for having a comparatively limited number of CPU cores, we expect to see the CPU trend continue.

If not for hardware limitations, it seems that the algorithm scales without bound on either the CPU or GPU. Overall, trends for the CPU and GPU are very similar. Because of these similarities, we will restrict ourselves to the GPU, but expect any conclusions to hold for the CPU as well.

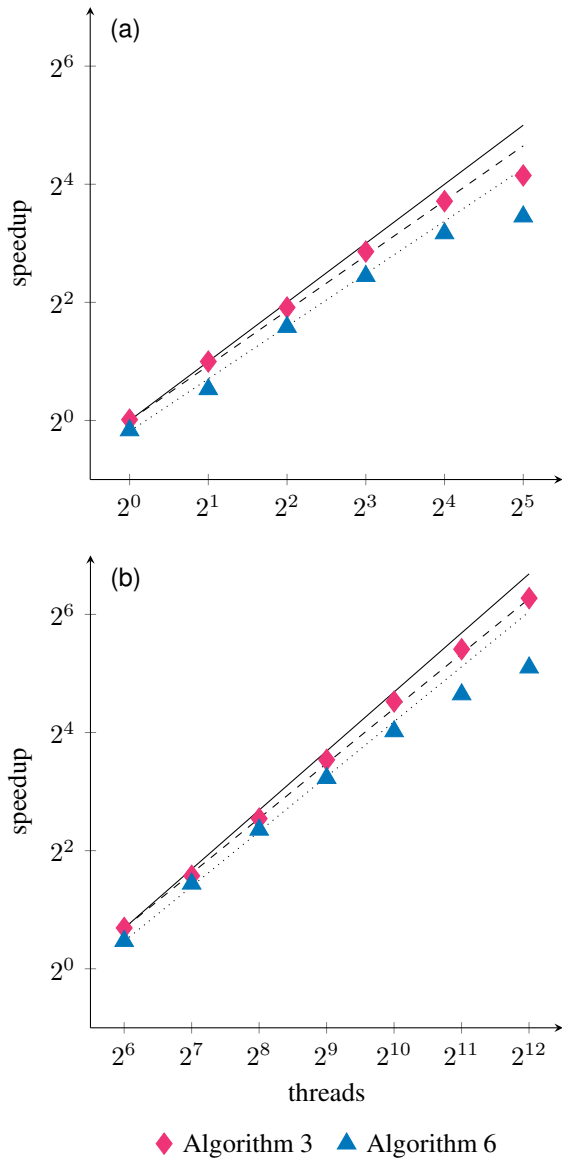
**4.1.3 Weak scaling** In contrast, with improved computing resources, we may wish to solve bigger problems. The ideal parallel algorithm solves a problem with  $p$  threads in the same time as it solves a twice bigger problem with  $2p$  threads. Here, we place between  $2^{16}$  and  $2^{19}$  points randomly in the domain. We increase the number of threads proportionally, between 128 and 1024.

Table 2 lists runtimes for increasing threads and problem size on the GPU. Interpolate scales nearly perfectly with a difference of 15 ms ( $\sim 3\%$ ) increase between the problem with 128 threads and  $2^{16}$  IB points and that with 1024 threads and  $2^{19}$  points. Spread, on the other hand, decreases in time as the problem size increases. This speedup is artificial, and should

**Table 2.** Weak scaling results for interpolation and spreading for  $p$  threads and  $n$  randomly placed IB points in a  $16\ \mu\text{m} \times 16\ \mu\text{m} \times 16\ \mu\text{m}$  triply periodic domain with  $h = 0.5\ \mu\text{m}$  on the GPU. Average time per call is reported in seconds.  $N$  is the number of samples taken.

$p$	$n$	interpolate	spread
		$N = 20000$	$N = 10000$
128	$2^{16}$	0.43930	0.47632
256	$2^{17}$	0.44918	0.46503
512	$2^{18}$	0.45072	0.44533
1024	$2^{19}$	0.45442	0.43561

not be expected in general. In the  $n = 2^{16}$  case, there is 1 IB point for every 4 grid cells, on average. When  $n = 2^{19}$ , the density increases to 2 for every grid cell. As a result, it becomes increasingly unlikely to find a cell containing no IB points. This means that writing the values to the output vector(s) becomes increasingly coalesced, which, in turn, reduces the number of writes to global memory and vastly improves the speed of the write overall. Typical use of the IB method does not have IB points in every grid cell, but the recommendations that IB points on connected structures be spaced  $0.5h-h$  apart typically yields 1–4 IB points in each occupied grid cell. We now consider a more typical use of the IB method.



**Figure 4.** Strong scaling results for Algorithm 6 and grid spacing  $h = 0.5 \mu\text{m}$  (a grid refinement of 64) for  $2^{16}$  randomly placed IB points in a  $16 \mu\text{m} \times 16 \mu\text{m} \times 16 \mu\text{m}$  triply periodic domain for (a) 1-32 CPU cores, and (b) 64-4096 threads on the GPU. Speedup is measured relative to serial Algorithms 3 and 2. The solid black lines show the trendline for ideal speedup. The dashed or dotted lines give the initial trend for interpolation and spreading, respectively.

## 4.2 Elastic objects

We are motivated by the desire to simulate the motion of cells immersed in a fluid. Cells are not randomly generated points, but cohesive structures, kept together by elastic forces and the near-constant volume enclosed by their membranes. In this section, we replace the randomly-placed IB points with points sampled on the surface of either a sphere or an RBC. We track  $n_d$  data sites per object, and interpolate fluid velocities only to these points. We construct an RBF interpolant based on the positions of the data sites and evaluate forces at  $n_s$  sample sites, chosen so that neighboring sample sites are initially within approximately  $0.5h$  of each other. We spread forces from the sample sites. It is generally the case that  $n_s > n_d$ , so that we interpolate to fewer points than we spread from.

In the parlance of Section 3,  $n_\gamma = n_d$  in the context of interpolation, and  $n_\gamma = n_s$  in the context of spreading. This violates the transpose property of Equations (8)–(9). Neither  $\mathcal{S}$  nor  $\mathcal{S}^\dagger$  are constructed explicitly, so the algorithms presented above work without modification. However, the  $\Gamma_h$  argument will differ between the spreading and interpolation algorithms. Data and sample sites are generated using the method described by Shankar et al. (2018). In this case, we invoke the fluid solver, so that as the object deforms, the force it imparts on the fluid will affect the fluid velocity. The sphere and RBC are elastic, obeying the Skalak constitutive law (Skalak et al. (1973)) with shear modulus  $2.5 \times 10^{-3} \text{ dyn/cm}$  and bulk modulus  $2.5 \times 10^{-1} \text{ dyn/cm}$ . The RBC has the reference configuration given in Omori et al. (2012):

$$\begin{aligned} x(\theta, \varphi) &= R_0 \cos \theta \cos \varphi, \\ y(\theta, \varphi) &= R_0 \sin \theta \cos \varphi, \\ z(\theta, \varphi) &= R_0 p(\cos \varphi) \sin \varphi, \end{aligned} \quad (16)$$

where  $\theta \in [-\pi, \pi]$ ,  $\varphi \in [-\pi/2, \pi/2]$ ,  $R_0 = 3.91 \mu\text{m}$ , and  $p(r) = 0.105 + r^2 - 0.56r^4$ . These tests require a timestep of  $k = 0.1 \mu\text{s}$  for stability. With  $\dot{\gamma} = 1000 \text{ s}^{-1}$ , an IB point requires at least 32 timesteps to transit a grid cell, so unlike the tests using randomly placed IB points above, there will be considerably more redundant computation. We first validate the fluid solver with the elastic sphere before performing scaling tests, similar to those above, with RBCs.

**4.2.1 Convergence study** To test the convergence of the fluid solver and cell representation, consider an object that obeys Skalak’s law with the coefficients given above and is spherical at rest. Deform the object from its rest configuration by stretching it by a factor of 1.1 in the  $z$  direction and compressing it by a factor of 1.1 in the  $y$  direction to maintain a fixed volume. For this test,  $\dot{\gamma}$  is zero, so the fluid velocity is initially zero, and the object tends toward its rest configuration over the course of simulation. We allow the object to relax for  $16 \mu\text{s}$ , and compare errors generated by successive grid refinements of 16, 32, 64, and 128 points per  $16 \mu\text{m}$ . For each grid, we use a fixed set of  $n_d = 625$  data sites, sampled approximately uniformly on the surface of the sphere, and choose  $n_s$  so that sample sites are approximately uniform and roughly  $h/1.1$  apart, so that sample sites are roughly  $h$  apart initially. For  $h = 1 \mu\text{m}$ ,  $n_s = 220$ , and a refinement by a factor of 2 increases  $n_s$  by a factor of 4, for a maximum number of 14080 sample sites for these tests. A thin interface which generates a force will cause a jump in the normal stress across the interface, which the IB method may not recover. We therefore anticipate first order convergence for the fluid velocity and data site positions.

Tables 3 and 4 show the convergence of fluid velocity and data sites, respectively. To compute errors in the fluid velocity, we construct a cubic spline from the velocities on the finer grid and evaluate the spline at the grid points of the coarser grid. Each of the interfaces is constructed with the same number of data sites, so the coordinates from one simulation to another can be compared directly. We recover approximately first order convergence for both fluid velocity and data sites positions. Having established asymptotic convergence of our IB solver, we continue by performing scaling tests with RBCs.

**Table 3.** Convergence of the fluid velocity for a deformed sphere returning to its rest configuration in a  $16\ \mu\text{m} \times 16\ \mu\text{m} \times 16\ \mu\text{m}$  triply periodic domain at  $t = 160\ \mu\text{s}$ . The finest grid, with  $h = 0.125\ \mu\text{m}$  uses timestep  $k = 0.025\ \mu\text{s}$ .

$h\ (\mu\text{m})$	$k\ (\mu\text{s})$	$\ \mathbf{u}_h - \mathbf{u}_{0.5h}\ _2$	order	$\ \mathbf{u}_h - \mathbf{u}_{0.5h}\ _\infty$	order
1.00	1.6	$2.2274 \times 10^{-2}$		$7.4187 \times 10^{-2}$	
0.50	0.4	$4.3280 \times 10^{-4}$	5.71513	$1.9083 \times 10^{-3}$	5.28079
0.25	0.1	$1.4684 \times 10^{-4}$	1.55951	$1.0847 \times 10^{-3}$	0.81497

**Table 4.** Convergence of data sites for a deformed sphere returning to its rest configuration in a  $16\ \mu\text{m} \times 16\ \mu\text{m} \times 16\ \mu\text{m}$  triply periodic domain at  $t = 16\ \mu\text{s}$ . For each grid, we track 625 data sites on the sphere. The finest grid, with  $h = 0.125\ \mu\text{m}$  used  $n_s = 14080$  sample sites.

$h\ (\mu\text{m})$	$n_s$	$\ \mathbf{X}_h - \mathbf{X}_{0.5h}\ _2$	order	$\ \mathbf{X}_h - \mathbf{X}_{0.5h}\ _\infty$	order
1.00	220	$2.9611 \times 10^{-3}$		$4.7812 \times 10^{-3}$	
0.50	880	$7.2997 \times 10^{-4}$	2.02020	$1.1687 \times 10^{-3}$	2.03253
0.25	3520	$3.5909 \times 10^{-4}$	1.02351	$6.0956 \times 10^{-4}$	0.93902

**4.2.2 Strong scaling** We again wish to see how these algorithms can help speed up the runtime of a fixed problem. Here, we consider tests with a single RBC and with 4 RBCs. To construct the RBCs, we now use  $n_d = 864$  data sites, for an initial data site spacing of approximately  $1.6h$ , and  $n_s = 8832$  sample sites per cell, for an initial sample site spacing of approximately  $0.5h$ . We use a timestep of  $k = 0.1\ \mu\text{s}$  to simulate the motion of the cells for 1 ms.

Figure 5 shows the speedup observed with increasing threads for 1 and 4 RBCs for 64–4096 threads on the GPU. We again see that the initial speedup for interpolation is nearly linear with increased threads. In subfigure 5(a), there is a sharp plateau that corresponds to every data site having its own thread. In other words, there are more threads than there is work to be done, since we track only 864 data sites for a single RBC. Subfigure 5(b), on the other hand, has 3456 data sites, so the trend continues for 512–4096 threads. In this case, we expect this graph to plateau beyond 4096, when each data site has its own thread. However, we do not expect for the trend to continue with more cells, as the presumed maximum number of threads for interpolation is 4480, as discussed in Section 4.1.2. Comparing subfigure 5(a) to (b), we see that the speedup in spreading is also dependent on the amount of work. This indicates that, as with interpolation, the maximum speedup for spreading is limited by hardware, rather than being a limitation of the algorithm.

The trendlines for these tests indicate that increasing computing resources by a factor of two decreases runtime by a factor of about 1.87 for these algorithms. Again, this is merely an approximation as the sort and reduction steps of the spreading algorithm are provided by `thrust`, and therefore are not limited to the listed number of threads. The similarity between the result of the tests with RBCs and with randomly placed points indicates that the distribution of points does not have a marked impact on the efficacy of the

**Table 5.** Weak scaling results for interpolate and spreading for increasing numbers of RBCs (cells column) and threads. Each RBC has  $n_d = 864$  and  $n_s = 8832$ . Average time per call is reported in seconds.  $N$  is the number of samples taken.

$p$	cells	interpolate $N = 20000$	spread $N = 10000$
64	1	0.01079	0.11881
128	2	0.01165	0.11219
256	4	0.01171	0.11214
512	8	0.01199	0.11354

parallelization for a fixed problem. We now see if the same holds for weak scaling tests.

**4.2.3 Weak scaling** To see how the algorithms scale given more computing resources, we increase the number of cells in the domain and the number of threads proportionally. We construct each cell with  $n_d = 864$  data sites and  $n_s = 8832$  sample sites, as before. We place between 1 and 8 cells in the domain, while threads increase from 64 to 512. Using a timestep of  $k = 0.1\ \mu\text{s}$ , we simulate the motion of these cells for 1 ms.

In Section 4.1.3, we observe that, as a side-effect of increasing point density per grid cell, runtime for spreading decreases as the number of points and threads increases. Here, the cells are initially far enough part as to not have any overlapping support points. As a result, while individual grid cells may contain several IB points, average point density is still low, so we do not expect to see the same reduction in runtime as observed previously.

Table 5 shows the runtimes for increasing number of RBCs and threads. We observe the near-perfect scaling we

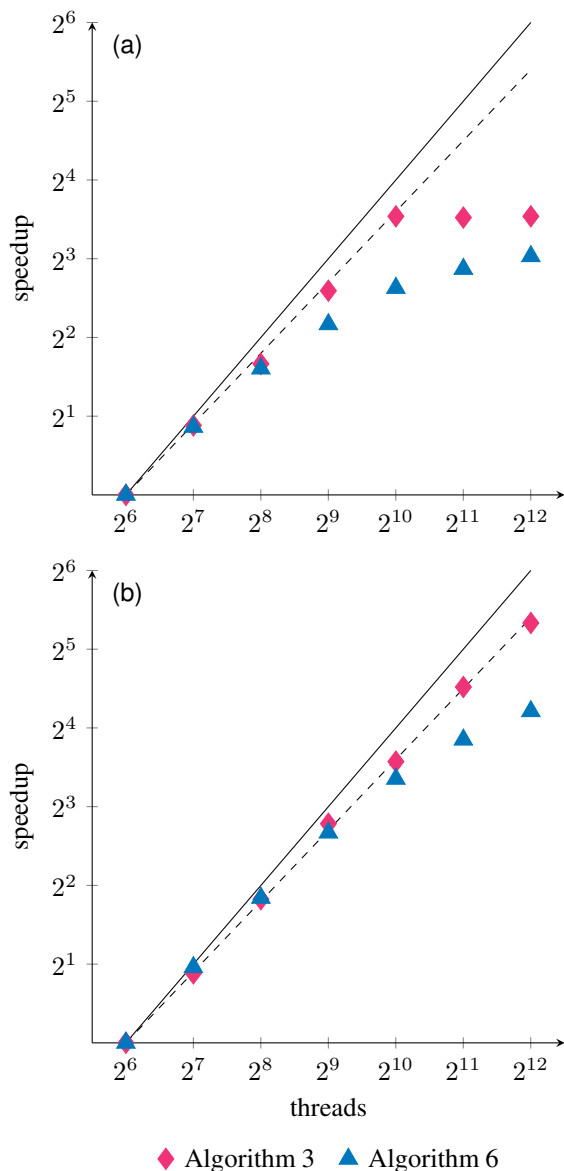


**Figure 5.** Speedup of Algorithms 3 and 6 with increasing numbers of threads compared to 64 threads on the GPU for (a) 1 and (b) 4 RBCs. Speedup is measured relative to the time taken for each algorithm using 64 threads on the GPU. Dashed lines indicate trends, and solid lines indicate ideal scaling.

saw with random IB points. For both interpolate and spread, we see that the runtimes are nearly constant: the slowest and fastest times differ by less than 2 ms and 7 ms, for interpolation and spread, respectively. After an initial drop in runtime between one RBC with 64 threads and two RBCs and 128 threads, runtimes even off and begin to increase, in contrast with the results in Section 4.1.3.

## 5 Summary

We presented Algorithm 3 for interpolation in parallel and introduced a novel parallel algorithm, Algorithm 4, for spreading forces from time-dependent interfaces in the immersed boundary method. These algorithms have a runtime that is independent of the Eulerian grid. This makes the parallelization useful for cases where IB points inhabit only a small percentage of the Eulerian grid cells.

We also introduced two variants for spread which trade off dependence on the Eulerian grid, in the form of a few vector adds and memory allocation, for improved runtimes for small enough grids.

These algorithms exhibit nearly ideal scaling, on both the CPU and GPU, for problems of fixed size and increasing number of threads, as well as for problems of increasing size and number of threads. We observed that on the GPU, larger problem sizes led to higher speedup plateaus, indicating that larger problems on more capable hardware will achieve even larger speedups than presented here.

It is instructive to compare Algorithm 4, which computes one value of  $\delta_h$  for each Lagrangian point per thread synchronization, with the parallelization of McQueen and Peskin (1997), which computes all values for  $\delta_h$  for a subset of the Lagrangian points each thread synchronization. Computing all values of  $\delta_h$  at the same time allows for minimizing calls to  $\phi$ , while processing all Lagrangian points simultaneously eliminates dependence on the background grid. It is straightforward to construct a pathological case for which McQueen and Peskin’s scheme performs poorly: if all of the Lagrangian points lie within the same  $s \times s$  columns of Eulerian grid cells, then a single thread processes all of the Lagrangian points, reducing the scheme to a serial one. The fine-grained approach in Algorithm 4 lacks this pathology, making it more robust to IB point configurations.

Though efficient load-balancing for Lagrangian work requires special techniques (Givelberg and Yelick (2006); Bhalla et al. (2019)), the worst-case scenario for distributed memory parallelizations has every Lagrangian object mapped to the same device (Erickson (2010)). For that reason, single-node results are still relevant. Nevertheless, we anticipate that our algorithms will perform well in multi-node systems as they do not rely on partitioning the Eulerian or Lagrangian points. Because information about the Eulerian grid is encoded by the functions  $\kappa$  and  $\#$ , an optimized distributed-memory algorithm may need to use a different  $\kappa$  or  $\#$  function on each node to account for Eulerian grid partitioning. As simulations become more computationally intensive, such algorithms will become more necessary. To that end, future work involves adapting our algorithms for multi-node and multi-GPU systems.

## Acknowledgements

The authors acknowledge useful discussions with Dr. Aaron Barrett.

## Declaration of conflicting interests

The authors have no conflicts of interest to declare.

## Funding

The author(s) disclosed receipt of the following financial support for the research, authorship, and/or publication of this article: This work was supported by the National Science Foundation [grant numbers DMS-1521748, DMS-176898, CISE CCF-1714844].

## References

- Bhalla APS, Nangia N, Dafnakis P, Bracco G and Mattiazzo G (2019) Simulating water-entry/exit problems using Eulerian-Lagrangian and fully-Eulerian fictitious domain methods within the open-source IBAMR library. *arXiv.org* : 1–32.
- Brown DL, Cortez R and Minion ML (2001) Accurate Projection Methods for the Incompressible Navier–Stokes Equations. *Journal of Computational Physics* 168(2): 464–499.
- Chuang PY, Mesnard O, Krishnan A and Barba LA (2018) PetIBM: toolbox and applications of the immersed-boundary method on distributed-memory architectures. *Journal of Open Source Software* 3(25): 558.
- Erickson LC (2010) *Blood Flow Dynamics: a Lattice Boltzmann Immersed Boundary Approach*. PhD Thesis, University of Utah, Salt Lake City.
- Fai TG, Griffith BE, Mori Y and Peskin CS (2013) Immersed Boundary Method for Variable Viscosity and Variable Density Problems Using Fast Constant-Coefficient Linear Solvers I: Numerical Method and Results. *SIAM Journal on Scientific Computing* 35(5): B1132–B1161.
- Fuselier EJ, Hangelbroek T, Narcowich FJ, Ward JD and Wright GB (2013) Kernel based quadrature on spheres and other homogeneous spaces. *Numerische Mathematik* 127(1): 57–92.
- Givberg E and Yelick K (2006) Distributed Immersed Boundary Simulation in Titanium. *SIAM Journal on Scientific Computing* 28(4): 1361–1378.
- Griffith BE (2009) An accurate and efficient method for the incompressible Navier–Stokes equations using the projection method as a preconditioner. *Journal of Computational Physics* 228(20): 7565–7595.
- Griffith BE (2011) Immersed boundary model of aortic heart valve dynamics with physiological driving and loading conditions. *International Journal for Numerical Methods in Biomedical Engineering* 28(3): 317–345.
- Griffith BE, Hornung RD, McQueen DM and Peskin CS (2007) An adaptive, formally second order accurate version of the immersed boundary method. *Journal of Computational Physics* 223(1): 10–49.
- Griffith BE, Hornung RD, McQueen DM and Peskin CS (2010) Parallel and Adaptive Simulation of Cardiac Fluid Dynamics. In: Parashar M and Li X (eds.) *Advanced Computational Infrastructures for Parallel and Distributed Adaptive Applications*. Hoboken, NJ, USA: John Wiley & Sons, Inc., pp. 105–130.
- Griffith BE and Luo X (2017) Hybrid finite difference/finite element immersed boundary method. *International Journal for Numerical Methods in Biomedical Engineering* 33: e2888.
- Griffith BE and Patankar NA (2020) Immersed Methods for Fluid–Structure Interaction. *Annual Review of Fluid Mechanics* 52(1): 421–448.
- Harlow FH and Welch JE (1965) Numerical Calculation of Time-Dependent Viscous Incompressible Flow of Fluid with Free Surface. *Physics of Fluids* 8(12): 2182–2189.
- Kassen A (2021) sonwell/ib.cu. URL <https://github.com/sonwell/ib.cu>.
- Layton SK, Krishnan A and Barba LA (2011) cuIBM – A GPU-accelerated Immersed Boundary Method. *arXiv.org*.
- Maxian O, Kassen AT and Strychalski W (2018) A continuous energy-based immersed boundary method for elastic shells. *Journal of Computational Physics* 371: 333–362.
- McQueen DM and Peskin CS (1997) Shared-Memory Parallel Vector Implementation of the Immersed Boundary Method for the Computation of Blood Flow in the Beating Mammalian Heart. *The Journal of Supercomputing* 11(3): 213–236.
- Mesnard O and Barba LA (2017) Reproducible and Replicable Computational Fluid Dynamics. *Computing in Science Engineering* 19(4): 44–55.
- Mittal R and Iaccarino G (2005) Immersed Boundary Methods. *Annual Review of Fluid Mechanics* 37(1): 239–261.
- Omori T, Ishikawa T, Barthès-Biesel D, Salsac AV, Imai Y and Yamaguchi T (2012) Tension of red blood cell membrane in simple shear flow. *Physical Review E* 86(5): 056321–056329.
- Patel S (2012) *aeroCuda: The GPU-Optimized Immersed Solid Code*. PhD Thesis, Harvard, Harvard University.
- Peskin CS (1972) *Flow patterns around heart valves: a digital computer method for solving the equations of motion*. PhD Thesis, Yeshiva University, New York.
- Peskin CS (2002) The immersed boundary method. *Acta Numerica* 11: 479–517.
- Shankar V, Kirby RM and Fogelson AL (2018) Robust Node Generation for Meshfree Discretizations on Irregular Domains and Surfaces. *SIAM Journal on Scientific Computing* 40(4): A2584–A2608.
- Shankar V, Wright GB, Kirby RM and Fogelson AL (2015) Augmenting the immersed boundary method with Radial Basis Functions (RBFs) for the modeling of platelets in hemodynamic flows. *International Journal for Numerical Methods in Fluids* 79(10): 536–557.
- Skalak R, Tozeren A, Zarda RP and Chien S (1973) Strain Energy Function of Red Blood Cell Membranes. *Biophysical Journal* 13: 245–264.
- Wesseling P (2001) *Principles of Computational Fluid Dynamics, Springer Series in Computational Mathematics*, volume 29. Berlin, Heidelberg: Springer Berlin Heidelberg.